

Support morphology-dependent alloying behaviour and interfacial effect of bimetallic Ni-Cu/CeO₂ catalysts

Yanan Liu,^{a,b} Alan J. McCue,^c Pengfei Yang,^{a,b} Yufei He,^{a,b} Lirong Zheng,^d Xingzhong Cao,^d Yi Man,^e Junting Feng,^{*,a,f} James A. Anderson,^{*,c} Dianqing Li^{a,b}

^a State Key Laboratory of Chemical Resource Engineering, Beijing University of Chemical Technology, Beijing, China

^b Beijing Engineering Center for Hierarchical Catalysts, Beijing University of Chemical Technology, Beijing 100029, China

^c Surface Chemistry and Catalysis Group, Department of Engineering, University of Aberdeen, Aberdeen, UK

^d Institute of High Energy Physics, Chinese Academy of Sciences, Beijing, China

^e Beijing Research Institute of Chemical Industry, Sinopec Group, Beijing, China

^f Beijing Advanced Innovation Center for Soft Matter Science and Engineering, Beijing University of Chemical Technology, Beijing, China

* Corresponding author

Address: Box 98, 15 Bei San Huan East Road, Beijing 100029, China

Tel: +86 10 64436992 Fax: +86 10 64436992

E-mail address: fengjt@mail.buct.edu.cn (Junting Feng);

j.anderson@abdn.ac.uk (James A. Anderson)

RESULTS AND DISCUSSIONS

As reported in Figure S1, the main patterns observed in four class of materials correspond to the (111), (200), (220), (311), and (222) planes of a pure cubic fluorite structure of ceria (space group *Fm3m*) as identified in line with JCPDS 34-0394. Noticeably, the reflection profiles vary as the shape of the nanoceria changing due to the texturization. For nanorods, the intensity ratio calculated using maximum height of the peak between diffractions of (220) and (200) increases from ~1.7 (a reference value for the bulk ceria) to a value of ~1.9. This rise illustrates that CeO₂-NR may grow along the [220] axis. Moreover, the calculated lattice parameters of conventional samples (Table S1) agree with that reported for bulk ceria (0.5411 nm), whereas shape-

controlled nanocerias display slightly lower value, which is associated with grain surface relaxation of small nanoparticles.¹ This is further confirmed by the average crystalline sizes determined from the reflections of (111) based on Scherrer equation (Table S1). HRTEM images were also collected on all nanomaterials to characterize the average size and shape. Figure 1A₁ exhibits the obvious aggregation of particles in CeO₂-CV with the size of ~24 nm, while ceria nanopolyhedron consists of uniform particles with a narrow size distribution in the range 9-15 nm; most of them are ~13 nm in Figure 1B. Furthermore, clear lattice fringes with interplanar spacing of 0.31 and 0.27 nm are observed in both samples, implying CeO₂-CV and CeO₂-NP are preferred to expose (111) and (200) facet. Also in this case, it is interesting to note from SAED that CeO₂-NP is of single-crystalline nature different from CeO₂-CV as polycrystalline, as shown in Figure 1A₃ and B₃. For the cube-like CeO₂ (Figure 1C), it is composed by nanocubes with a basically homogeneous particle size distribution (13-27 nm). The corresponding magnified image (Figure 1C₂) presents the lattice spacing of 0.27 nm, revealing that only (200) facet exists in the CeO₂-NCs. Figure 1D displays a well-distributed nanorods with the diameter of 15 nm but a wide distribution of length varying between 7 and 33 nm. In this case, a domain oriented along the [110] direction is monitored with the corresponding (220) planes of ceria. The above conclusion is in conformance with XRD analysis.

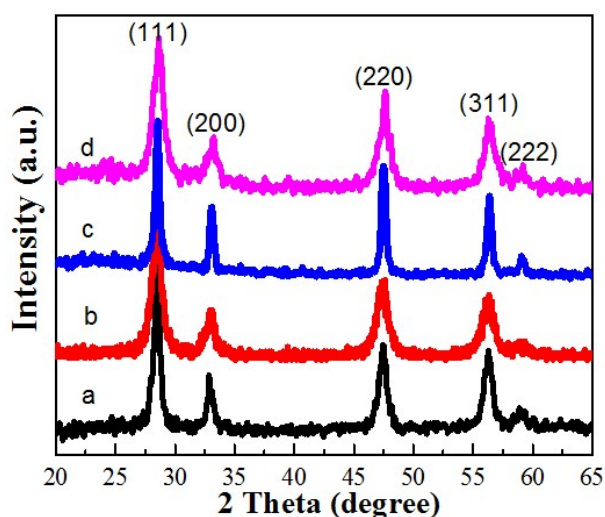


Figure S1. XRD of (a) polycrystalline conventional CeO₂ (CV), (b) nanopolyhedron CeO₂ (NP), (c) nanocube CeO₂ (NC) and (d) nanorod CeO₂ (NR).

Table S1 Properties of CeO₂ supports with different facets

Supports	CeO ₂ -CV	CeO ₂ -NP	CeO ₂ -NC	CeO ₂ -NR
Particle size (nm) ^a	24.4	13.2	19.8	15.0
Particle size (nm) ^b	31.7	17.8	33.8	16.5
Lattice parameters (nm) ^b	0.5411	0.5408	0.5409	0.5409
BET surface area (m ² g ⁻¹)	68	61	43	79
Pore volume (cm ³ /g)	0.20	0.12	0.14	0.28
Pore size (nm)	9.8	6.9	10.0	10.8

^a Determined by HRTEM.

^b Calculated based on (111) facet in XRD result.

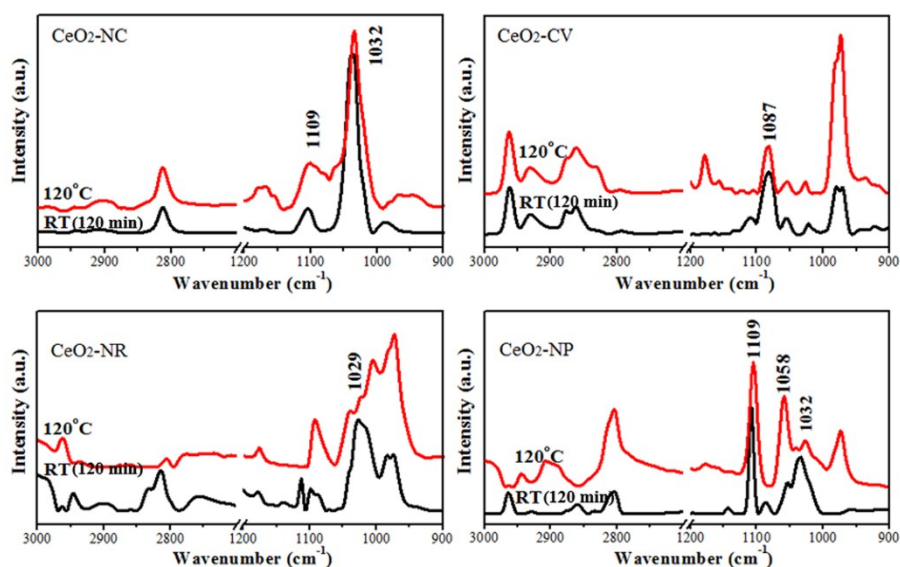


Figure S2. IR spectra of methanol desorption on ceria at room temperature and 120°C.

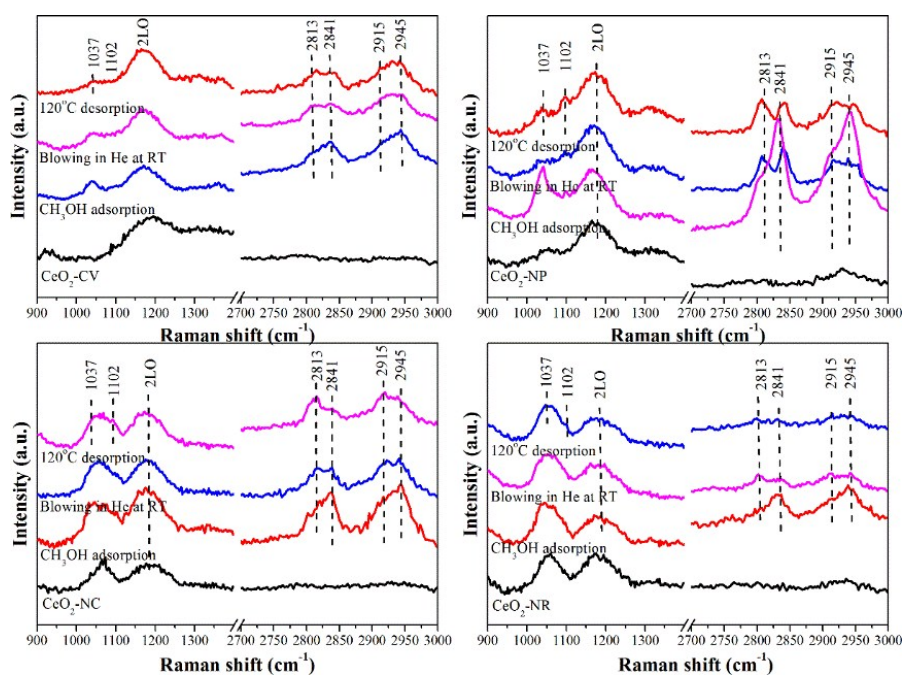


Figure S3. Raman spectra following methanol adsorption and desorption on ceria at room temperature and 120°C.

As in Figure S4, the morphology for these four substrates was well preserved after the incorporation of active species. Random selection of 200 particles in different regions (Figure S4 insets) are carried out to measure the mean size and distribution. For Ni-Cu/CeO₂-NP, the average size is found to be 2.6 nm, which is smaller than those of Ni-Cu/CeO₂-CV (4.3 nm), while the average sizes observed in Ni-Cu/CeO₂-NC and Ni-Cu/CeO₂-NR are quite close, ~3.5 nm. Additionally, the metal dispersion of all catalysts was surveyed by CO-chemisorption, although the stoichiometric ratio of M/CO is complicate and controversial. However in our system, CO/M=1:1 is assumed based on the studies.^{2,3} The obtained data summarized in Table S2 clearly display the sequence as follow: Ni-Cu/CeO₂-NP>Ni-Cu/CeO₂-NC>Ni-Cu/CeO₂-NR>Ni-Cu/CeO₂-CV, which is consistent with the trends from HRTEM analysis. By closely magnifying the TEM images, the direct connection of a quantity of metal nanoparticles in the truncated octahedral at the edge of the nanopolyhedron CeO₂ is noticed.

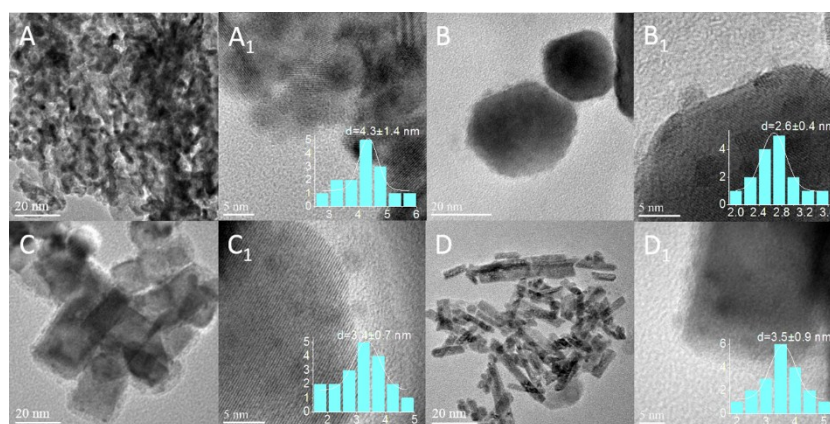


Figure S4. HRTEM of (A) Ni-Cu/CeO₂-CV, (B) Ni-Cu/CeO₂-NP, (C) Ni-Cu/CeO₂-NC, (D) Ni-Cu/CeO₂-NR and the distribution of particle size in the inset.

Table S2 Properties of Ni-Cu/CeO₂ catalysts with different facets and quantitative analyses for Ni-Ni contributions to the EXAFS data[§]

Samples	Ni-Cu/CeO ₂	Ni-Cu/CeO ₂	Ni-Cu/CeO ₂	Ni-Cu/CeO ₂
	-CV	-NP	-NC	-NR
Ni loading (wt. %)	4.7	4.7	4.7	4.8
Cu loading (wt. %)	4.4	4.9	4.8	4.7

Dispersion (%) ^a	20.4	33.8	26.7	25.1
Dispersion (%) ^b	21.5	35.1	27.8	27.3
TOF (s ⁻¹) ^c	0.0016	0.0070	0.0058	0.0036
CN ^d	8.0±0.9	7.6±1.1	8.5±1.4	8.1±1.2
R ^e (Å)	2.50	2.54	2.51	2.52
Σ ^f	0.0039	0.0057	0.0081	0.0063

^a Determined by HRTEM.

^b Determined by CO pulse.

^c TOF value estimated at 30°C in the gas reaction.

^d Coordination number (N).

^e Atomic distance (r).

^f Debye-Waller factor (σ).

^g Ni foil is used as reference with the coordination number of 12 and atomic distance of 2.49 Å

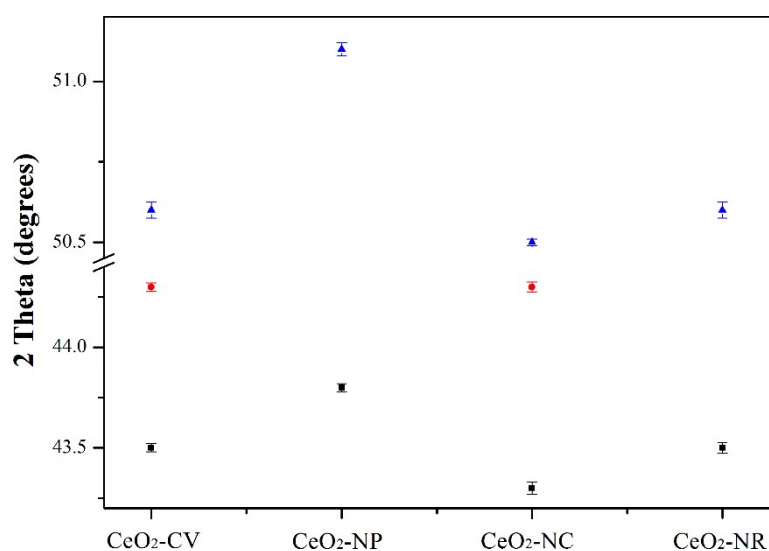


Figure S5 Variation of the position diffraction peak for CeO₂-CV, CeO₂-NP, CeO₂-NC and CeO₂-NR supported Ni-Cu catalysts. Error bars represent the standard deviation of five measurements.

Table S3 Ni-Cu/CeO₂-C500 precursors with different facets and quantitative analyses for Ni-O contributions to the EXAFS data ^f

Precursors	Ni-Cu/CeO ₂ -	Ni-Cu/CeO ₂ -	Ni-Cu/CeO ₂ -	Ni-Cu/CeO ₂ -
	CV-C500	NP-C500	NC-C500	NR-C500
Lattice parameters (nm) ^a	0.5410±0.0002	0.5407±0.0002	0.5400±0.0003	0.5404±0.0002
BET surface area (m ² g ⁻¹) ^b	59	53	36	60
Pore volume (cm ³ /g)	0.18	0.09	0.14	0.17
Pore size (nm)	9.2	4.5	15.7	7.7
CN ^c	-	6.1±0.4	5.6±0.7	-
R ^d (Å)	-	2.11	2.15	-
σ ^e	-	0.0073	0.0051	-

^a Calculated based on (111) facet in XRD result.

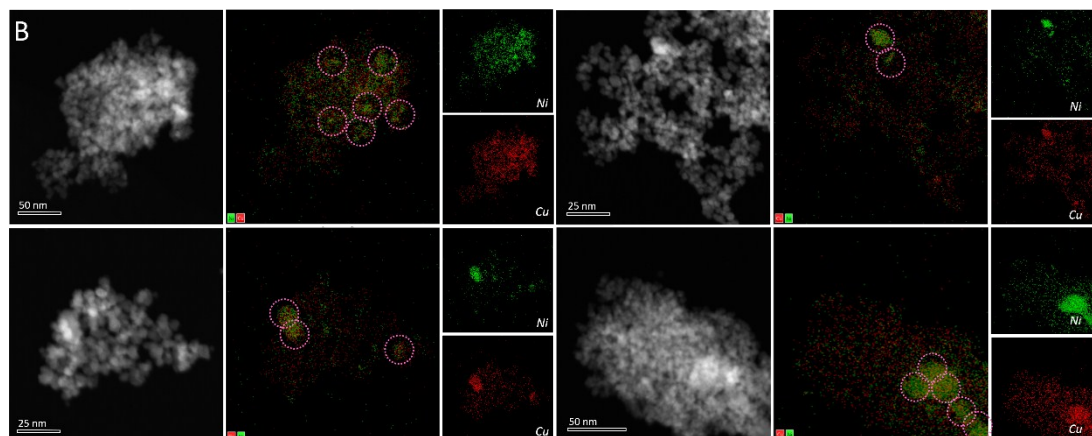
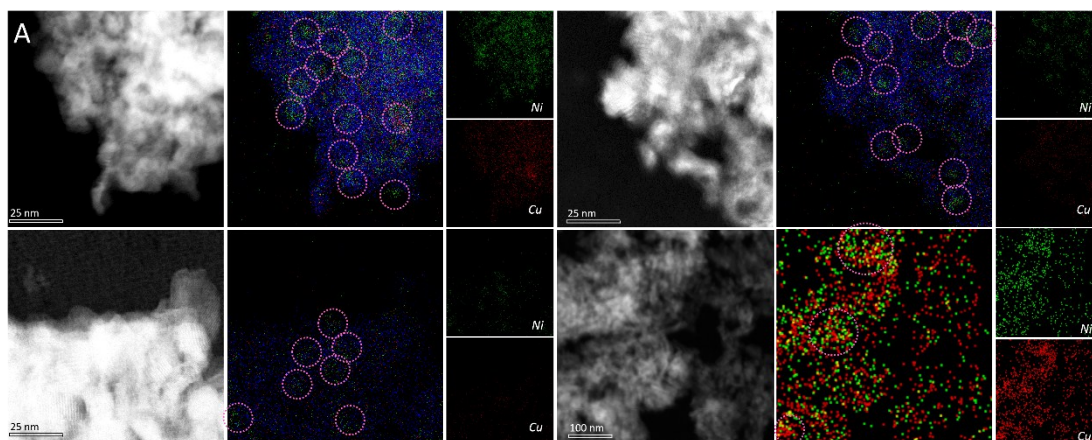
^b Determined by BET.

^c Coordination number (N).

^d Atomic distance (r).

^e Debye-Waller factor (σ).

^f NiO is used as reference with the coordination number of 6 and atomic distance of 2.08 Å



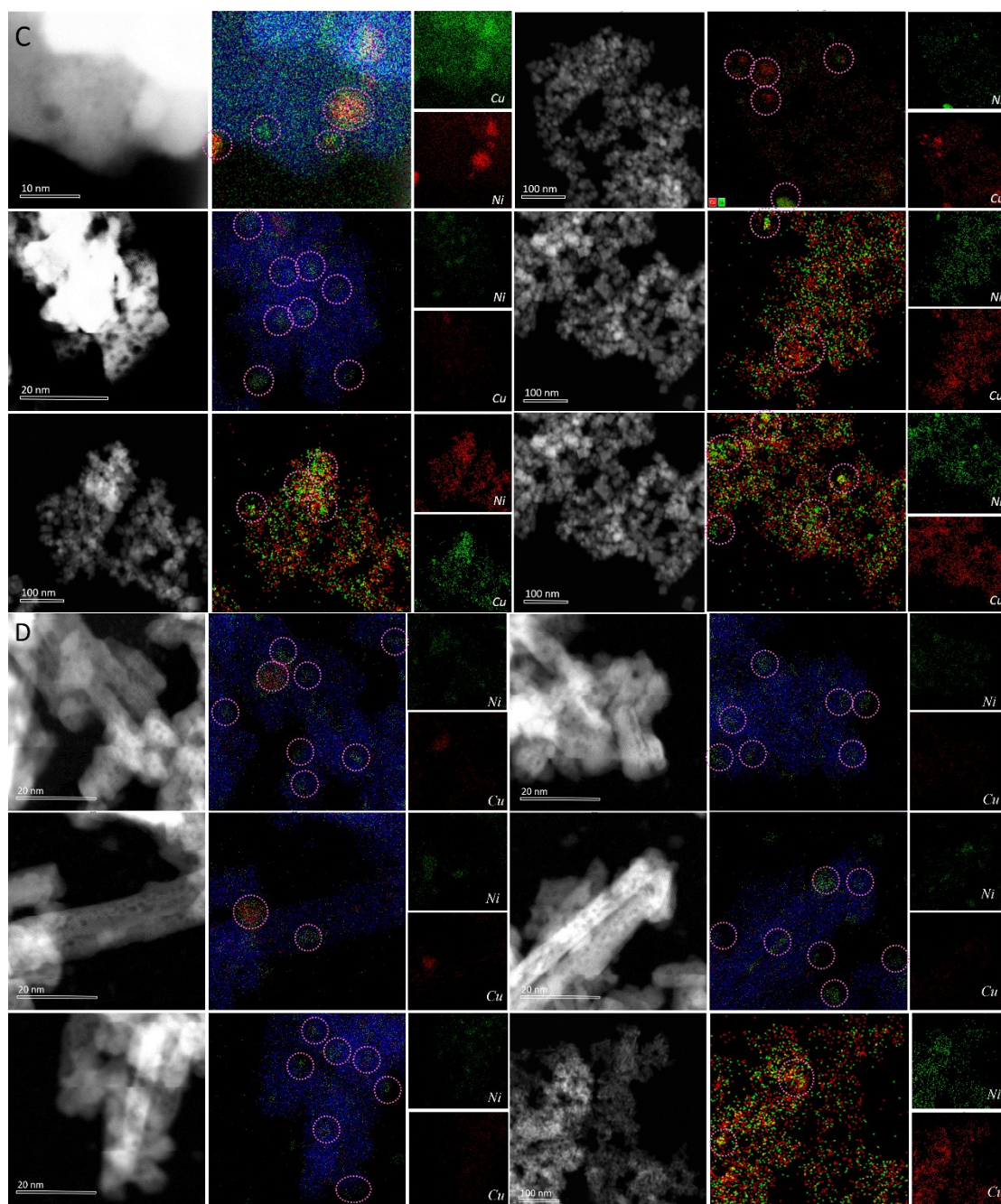


Figure S6. Aberration-corrected HAADF-STEM of (A) Ni-Cu/CeO₂-CV (B) Ni-Cu/CeO₂-NP (C) Ni-Cu/CeO₂-NC (D) Ni-Cu/CeO₂-NR catalysts.

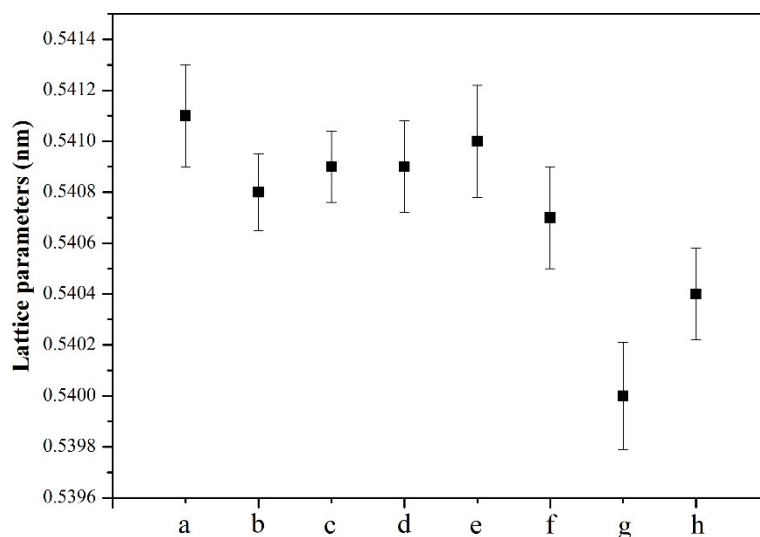


Figure S7 The observed variation of lattice parameter for (a) CeO₂-CV, (b) CeO₂-NP, (c) CeO₂-NC, (d) CeO₂-NR, (e) Ni-Cu/CeO₂-CV-C500, (f) Ni-Cu/CeO₂-NP-C500, (g) Ni-Cu/CeO₂-NC-C500 and (h) Ni-Cu/CeO₂-NR-C500. Error bars represent the estimated standard deviations of the experimental values.

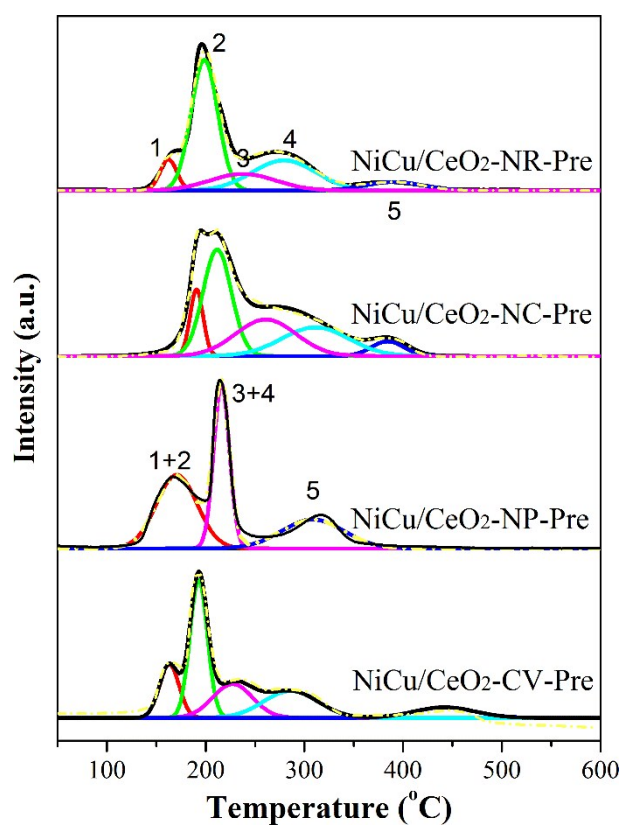


Figure S8 The deconvolution of the TPR profiles over NiCu samples

Table S4 hydrogen consumption of NiCu samples derived from TPR

Samples	Moles of consumed H ₂ (μmol H ₂ /g)
---------	-----------------------------------------------------------

	Zone 1 Peak 1+2	Zone 2 Peak 3+4	Zone 3 Peak 5	Total
NiCu/CeO ₂ -CV-Pre	654	745	148	1547
NiCu/CeO ₂ -NP-Pre	670	800	392	1862
NiCu/CeO ₂ -NC-Pre	633	713	254	1600
NiCu/CeO ₂ -NR-Pre	585	648	337	1570

XPS peaks (Figure S9A) of all the Cu containing catalysts centred at ca. 932.7 eV is owing to Cu (0) species, and the peak at 935.2 eV corresponds to Cu²⁺ species with the associated shakeup satellite peak at 942.6 eV. The Cu⁺ peak is not included in this analysis due to overlap with the position of Cu⁰. For the monometallic Cu catalysts, we observe that the binding energy (BE) of Cu⁰, with respect to Cu metal (932.9 eV), shifts to lower BE, which is likely driven by charge transfer from Ce³⁺ to Cu, indicating an interaction of CeO₂ support with metal. Moreover, Ni XPS spectra of all the relative catalysts is given with three peaks between 852.2 and 853.0 eV, 853.5 and 854.0 eV, 854.6 and 854.9 eV that are assigned to metallic Ni⁰, the interacted NiO with support, and NiO, respectively. By analysis of Ni 2p spectra of monometallic material (Figure S9B), the shift to lower binding energies for Ni⁰ 2p_{3/2} peaks is in the order Ni-Cu/CeO₂-NP > Ni-Cu/CeO₂-NC > Ni-Cu/CeO₂-NR ≈ Ni-Cu/CeO₂-CV, resulting from the proverbial interactions between Ni and CeO₂ caused by charge transfer from reducible Ce species to Ni d-states.

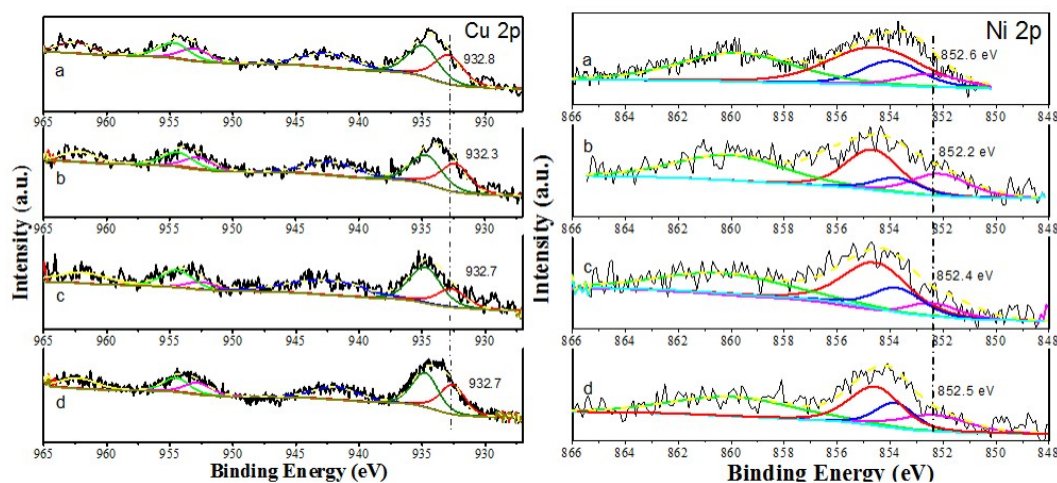


Figure S9. XPS spectra of (A) Cu 2p over (a) Cu/CeO₂-CV, (b) Cu/CeO₂-NP, (c) Cu/CeO₂-NC and (d) Cu/CeO₂-NR; (B) Ni 2p 3/2 over (a) Ni/CeO₂-CV, (b) Ni/CeO₂-NP, (c) Ni/CeO₂-NC and (d) Ni/CeO₂-NR.

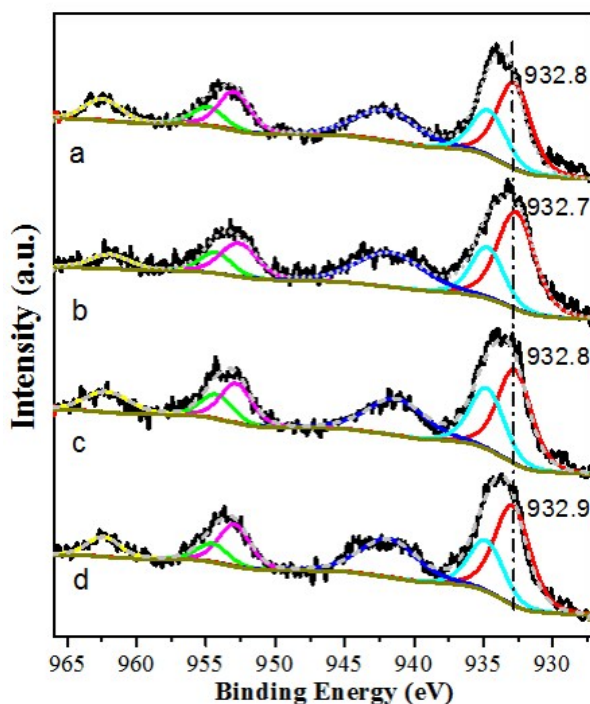


Figure S10. XPS spectra of Cu 2p over (a) Ni-Cu/CeO₂-CV, (b) Ni-Cu/CeO₂-NP, (c) Ni-Cu/CeO₂-NC and (d) Ni-Cu/CeO₂-NR

To further understand the interaction between metal and support, the Raman spectra of catalysts was also determined (Figure S11B). The relative intensity of $I(D)/I(F_{2g})$ is somewhat higher in all the catalysts in comparison to the pristine CeO₂ (Figure S11A). More interestingly, a significant increase occurs for the $I_D/I_{F_{2g}}$ value in the case of Ni-Cu/CeO₂-NP samples, much superior to CeO₂-NC, CeO₂-NR, and CeO₂-CV supported Ni-Cu catalysts, whereas it shows lower ratio of $I_D/I_{F_{2g}}$ in the support. This indicates the vital role of reduction process and metal inducement in the formation of oxygen vacancies. Similarly, Positron annihilation spectroscopy also provide the same trend of the oxygen vacancies as Raman measurement. In comparison with that of pure ceria (Table S5), the I_2/I_1 ratio in Table S6 on behalf of the relative concentration of oxygen vacancy increases in the order of Ni-Cu/CeO₂-NP (1.30) > Ni-Cu/CeO₂-NR (0.99) > Ni-Cu/CeO₂-NC (0.82) > Ni-Cu/CeO₂-CV (0.74). The data imply that the Ni-Cu species with atomically arranged Ni and Cu in the sense of nanopolyhedron enhances the reduction degree of CeO₂-NPs, favour to the production of abundant surface defects, in comparison with Ni-Cu/CeO₂-NRs and Ni-Cu/CeO₂-NCs.

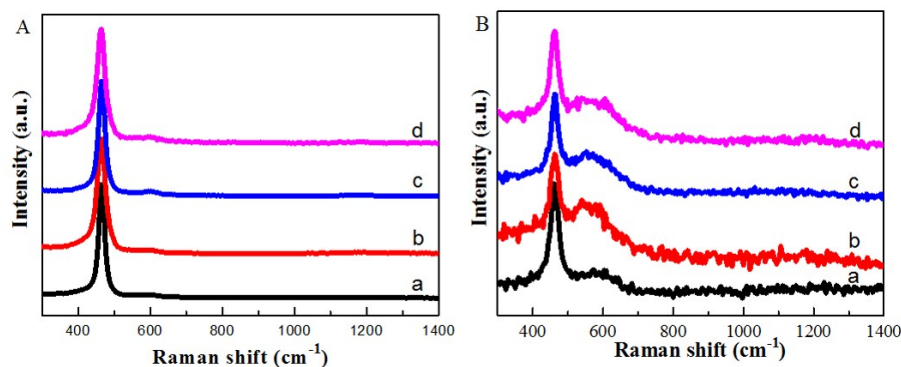


Figure S11. Raman of (A) (a) CeO₂-CV, (b) CeO₂-NP, (c) CeO₂-NC, (d) CeO₂-NR and (B) the corresponding catalysts.

Table S5 Positron lifetimes and relative intensities of the supports.

Samples	CeO ₂ -CV	CeO ₂ -NP	CeO ₂ -NC	CeO ₂ -NR
$\tau 1^a$ (ps)	172.9	162.0	180.7	189.7
I1 (%)	59.8	64.7	53.1	65.6
$\tau 2^b$ (ps)	326.2	318.4	3480	397.0
I2 (%)	31.7	37.5	35.0	46.6
$\tau 3^c$ (ns)	2.55	2.40	2.89	3.05
I3 (%)	2.3	2.6	2.1	2.2
I2/I1	0.53	0.58	0.66	0.71

Table S6 Positron lifetimes and relative intensities of the catalysts.

Samples	Ni-Cu/CeO ₂ -CV	Ni-Cu/CeO ₂ -NP	Ni-Cu/CeO ₂ -NC	Ni-Cu/CeO ₂ -NR
$\tau 1$ (ps)	185.3	182.9	182.9	191.7
I1 (%)	56.5	42.9	53.7	49.2
$\tau 2$ (ps)	392.4	395.8	390.0	402.1
I2 (%)	41.3	54.6	44.2	48.8
$\tau 3$ (ns)	2.65	2.45	2.97	3.14
I3 (%)	2.1	2.5	2.1	2.0
I2/I1	0.74	1.30	0.82	0.99

^a the shortest-lived one ($\tau 1$) arising from small neutral Ce³⁺-oxygen vacancy, mainly exist in the bulk section.

^b the intermediate components 2 is probably caused by larger-size defective sites (i.e., dimmers or larger).

^c the longest component ($\tau 3$) is attributed to the annihilation of ortho-positronium atoms produced in the large voids of the material.

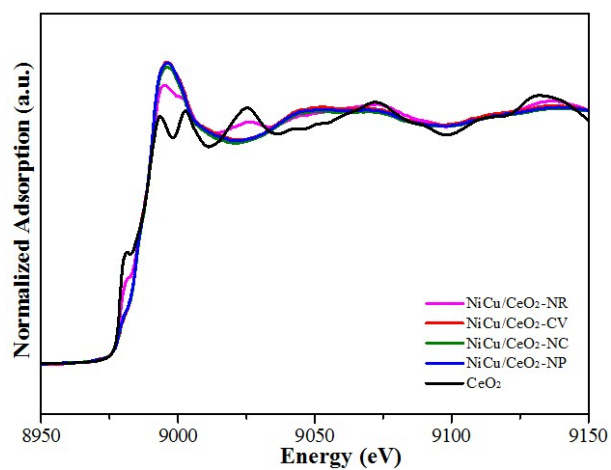


Figure S12. Cu K-edge XANES spectra over NiCu materials.

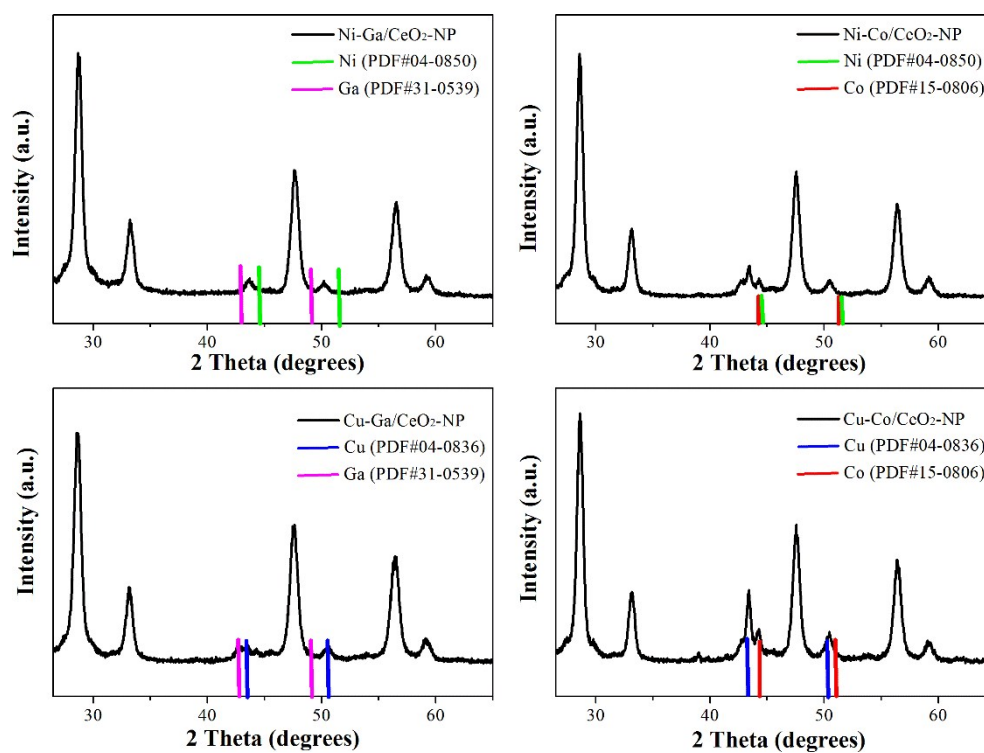


Figure S13. XRD profiles of CeO₂-NP supported bimetallic Ni-Ga, Ni-Co, Cu-Ga and Cu-Co catalysts

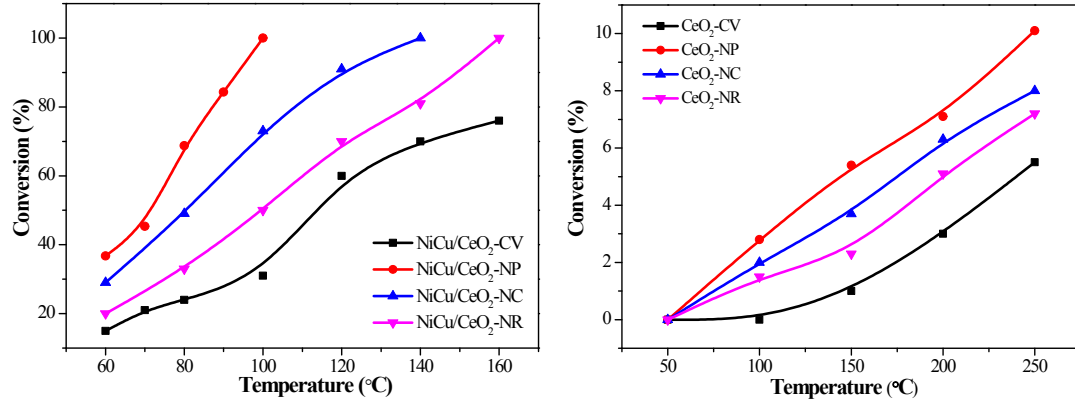


Figure S14. Conversion of (A) Ni-Cu catalysts (B) pristine CeO₂ after 5 h time on stream.

Mass and Heat Transfer Calculations for acetylene hydrogenation on Ni-Cu/CeO₂ catalysts.

(T=373K, acetylene conversion ~100%, P = 1 bar)

Mears Criterion for External Diffusion (Fogler, p841; Mears, 1971)

If $\frac{-r_A' \rho_b R n}{k_c C_{Ab}} < 0.15$, then external mass transfer effects can be neglected.

$-r_A'$ = reaction rate, kmol/kg·cat·s

n = reaction order

R = catalyst particle radius, m

ρ_b = bulk density of catalyst bed, kg/m³

ρ_c = solid catalyst density, kg/m³

C_{Ab} = bulk gas concentration of A, kmol/m³

k_c = mass transfer coefficient, m/s

Sherwood number (Sh) = $k_c(2R_p)/D_{AB}$

$Sh = 2 + 0.6Re^{1/2}Sc^{1/3}$

Reynolds number (Re) = $2U \cdot R \cdot \rho / \mu$ (where U is superficial velocity in m/s, ρ is the density of the reactant mixture fluid, estimated using C₂H₂/N₂ at 373K, μ is the viscosity of the reactant mixture fluid, estimated using C₂H₂/N₂ at 373K)

Schmidt number (Sc) = $\mu/\rho \cdot D_{AB}$

$D_{AB} = 18.583 T^{1.5} [(M_1 + M_2) / M_1 M_2]^{0.5} / P \cdot \sigma_{12}^2 \Omega$ (where D_{AB} is gas-phase diffusivity in m^2/s , T is temperature in K, M is the molecular mass in kg/kmol, P is the pressure in bar, Ω is collision integral, σ_{12} is constant of Lennard-Jones potential energy function.

$$\frac{-r'_A \rho_b R n}{k_c C_{Ab}} = [4.13 \times 10^{-6} \text{ kmol/kg}\cdot\text{s}] [278 \text{ kg/m}^3] [1.5 \times 10^{-6} \text{ m}] [0.6] / ([3.94 \text{ m/s}] [6.65 \times 10^{-4} \text{ kmol/m}^3]) = \mathbf{3.9 \times 10^{-7} < 0.15 \text{ \{Mears for External Diffusion\}}}$$

Weisz-Prater Criterion for Internal Diffusion (Fogler, p839)

If $C_{WP} = \frac{-r'_{A(obs)} \rho_c R^2}{D_e C_{As}} < 1$, then internal mass transfer effects can be neglected.

$-r'_{A(obs)}$ = observed reaction rate, kmol/kg·cat·s

R = catalyst particle radius, m

ρ_c = solid catalyst density, kg/m³;

D_e = effective gas-phase diffusivity, m²/s [Fogler, p815]

$$= \frac{D_{AB} \phi_p \sigma_c}{\tau} \text{ where}$$

D_{AB} = gas-phase diffusivity m²/s; ϕ_p = pellet porosity; σ_c = constriction factor;

τ = tortuosity.

C_{As} = gas concentration of A at the catalyst surface, kmol-A/m³

$$C_{WP} = \frac{-r'_{A(obs)} \rho_c R^2}{D_e C_{As}} = [4.13 \times 10^{-6} \text{ kmol/kg}\cdot\text{s}] [722 \text{ kg/m}^3] [1.5 \times 10^{-6} \text{ m}]^2 / ([8.36 \times 10^{-9} \text{ m}^2/\text{s}] [6.65 \times 10^{-4} \text{ kmol/m}^3]) = \mathbf{1.2 \times 10^{-3} < 1}$$

\{Weisz-Prater Criterion for Internal Diffusion\}

Mears Criterion for External (Interphase) Heat Transfer (Fogler, p842)

$$\left| \frac{-\Delta H_r (-r'_A) \rho_b R E}{h_t T_b^2 R_g} \right| < 0.15$$

$$\text{Nusselt number (Nu)} = 2 + 0.6\text{Re}^{1/2}\text{Sc}^{1/3}$$

$$\text{Nu} = h_t(2R_p)/\lambda$$

$$[176 \text{ kJ/mol} \times 4.13 \times 10^{-3} \text{ mol/kg} \cdot \text{s} \times 278 \text{ kg/m}^3 \times 1.5 \times 10^{-6} \text{ m} \times 30 \text{ kJ/mol}] / [22.4 \text{ kJ/m}^2 \cdot \text{K} \cdot \text{s} \times 373^2 \text{ K}^2 \times 8.314 \times 10^{-3} \text{ kJ/mol} \cdot \text{K}] = \mathbf{3.8 \times 10^{-7} < 0.15}$$

{Mears Criterion for External (Interphase) Heat Transfer}

Mears Criterion for Combined Interphase and Intraparticle Heat and Mass Transport (Mears, 1971)

$$\frac{-r'_A R^2}{C_{Ab} D_e} < \frac{1 + 0.33\gamma\chi}{|n - \gamma_b \beta_b| (1 + 0.33n\omega)}$$

$$\gamma = \frac{E}{R_g T_s}; \quad \gamma_b = \frac{E}{R_g T_b}; \quad \beta_b = \frac{(-\Delta H_r) D_e C_{Ab}}{\lambda T_b}; \quad \chi = \frac{(-\Delta H_r) - r'_A R}{h_t T_b}; \quad \omega = \frac{-r'_A R}{k_c C_{Ab}}$$

γ = Arrhenius number; β_b = heat generation function;

λ = catalyst thermal conductivity, W/m·K;

χ = Damköhler number for interphase heat transport

ω = Damköhler number for interphase mass transport

$$\frac{-r'_A R^2}{C_{Ab} D_e} = [4.13 \times 10^{-6} \text{ kmol/kg} \cdot \text{s} \times (1.5 \times 10^{-6})^2 \text{ m}^2] / [6.65 \times 10^{-4} \text{ kmol/m}^3 \times 8.36 \times 10^{-9}$$

$$\text{m}^2/\text{s}] = 1.7 \times 10^{-6} < 1.67$$

{Mears Criterion for Interphase and Intraparticle Heat and Mass Transport}

Table S7 Parameters used in the Mears criterion and Weisz-Prater Criterion for estimating mass and heat transfer limitations in semi-hydrogenation of acetylene

Parameters	Value
Reaction rate at 373 K: $-r_A$ (kmol/kg _{cat} s)	$\sim 4.13 \cdot 10^{-6}$

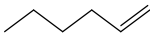
Density of catalyst: $\rho_c(\text{Kg/m}^3)$	~ 722
Catalyst bed density: $\rho_b(\text{Kg/m}^3)$	~ 278
Radius of catalyst: $R(\text{m})$	$\sim 1.50 \cdot 10^{-6}$
Radius of quartz tube: $r(\text{m})$	$\sim 3.50 \cdot 10^{-3}$
Reaction order: $n_{(\text{C}_2\text{H}_2)}$	~ 0.6
Bulk gas concentration of C_2H_2 at 373 K: $C_{Ab}(\text{kmol/m}^3)$	$\sim 6.65 \cdot 10^{-4}$
Viscosity of the reactant at 373 K: $(\mu_{\text{C}_2\text{H}_4})/(\mu_{\text{N}_2})(\text{Pa}\cdot\text{s})$	$\sim 1.26 \cdot 10^{-5}/2.10 \cdot 10^{-5}$
Viscosity of the reactant mixture fluid at 373 K: $\mu(\text{Pa}\cdot\text{s})^a$	$\sim 1.47 \cdot 10^{-5}$
Density of reactant mixture fluid at 373 K: $\rho(\text{Kg/m}^3)^b$	~ 0.94
Re	$\sim 1.39 \cdot 10^{-2}$
Sc	~ 2.78
Sh	~ 2.10
Gas-phase diffusivity: $D_{AB}(\text{m}^2/\text{s})$	$\sim 5.63 \cdot 10^{-6}$
Mass transfer coefficient: $k_c(\text{m/s})$	~ 3.94
Effective gas-phase diffusivity: $D_e(\text{m}^2/\text{s})$	$\sim 8.36 \cdot 10^{-9}$
Heat of reaction: $\Delta H_r(\text{kJ/mol})$	~ 176
Activation energy: $E(\text{kJ/mol})$	~ 30
Thermal conductivity at 373 K: $\lambda_{\text{C}_2\text{H}_4}/\lambda_{\text{N}_2}(\text{W/m}\cdot\text{K})$	$\sim 3.23 \cdot 10^{-2}/3.15 \cdot 10^{-2}$
Thermal conductivity of reactant mixture fluid at 373 K: $\lambda(\text{W/m}\cdot\text{K})^c$	$\sim 3.20 \cdot 10^{-2}$
Nu	~ 2.10
Heat transfer coefficient: $h_t(\text{W/m}^2\cdot\text{K})$	$\sim 2.24 \cdot 10^4$

^a estimated based on Wilke formula

^b estimated based on gas component

^c estimated based on Wassiljewa calculation method

Table S8 Comparison of catalytic performance over Ni-based catalysts.

Catalysts	Main product	Conv. (%)	Sel. (%)	T (°C)	P (MPa)	H ₂ /C ₂ H ₂ (Alkyne/M)
Ni-Cu/CeO ₂ -NP		100	72.7	225	0.1	4
pre-Ni-Cu/MMO ⁴		86	61	220	0.4	2
Cu _{2.75} Ni _{0.25} Fe ⁵		100	80	250	0.1	3
NiCu/SiO ₂ ⁶	H-C=C-H	97	<40	120	-	4
Ni ₅ Zn ₂₁ ⁷		75	50	160	0.01	10
NiZn/MgAl ₂ O ₄ ⁸		75	53	120	-	10
Ni/SiO ₂ ⁹		75	<40	80	-	10
Ni/Al ₂ O ₃ ¹⁰		12	55	200	0.1	3
Ni-Cu/CeO ₂ -NP		>99	92.7	100	0.55	116
N modified Pd ¹¹		25	98.5	30	1.05	887
Bi modified Pd ¹²		Yield 88		25	-	1300
Pd NPs ¹³		85	96.5	30	0.28	2700
pre-Ni-Cu/MMO ⁸		94.3	90.7	100	0.55	53

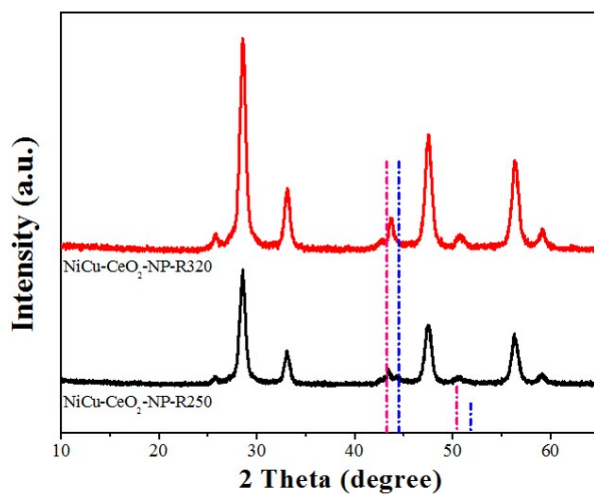


Figure S15. XRD profiles of Ni-Cu/CeO₂-NP reduced at 250°C and 320°C.

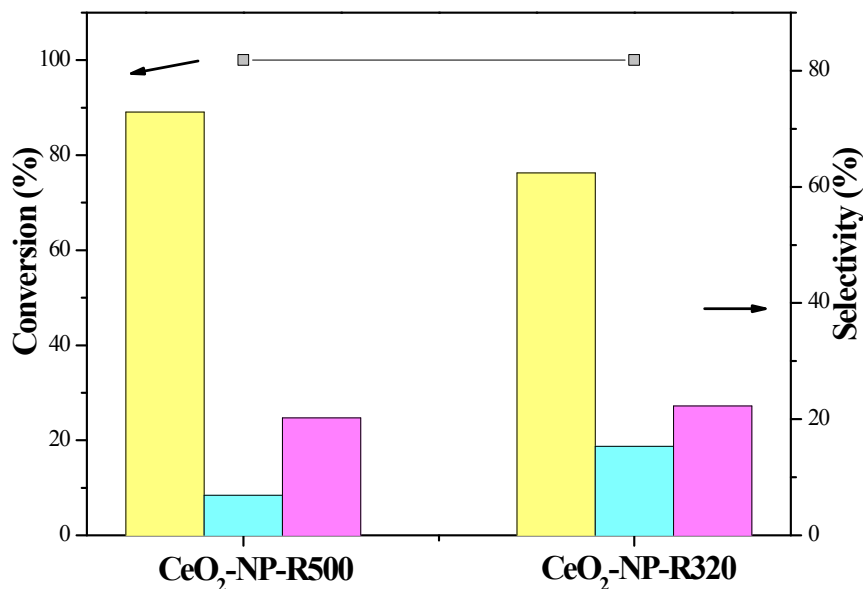


Figure S16. Catalytic behaviour of Ni-Cu/CeO₂-NP reduced at 500°C and 320°C.

The adsorption isotherms of H₂ on this series of Ni-Cu/CeO₂ catalysts meets Langmuir model, and thus these adsorption systems was fitted using linear Langmuir isotherm.¹⁴ The correlation coefficients ($R^2 > 0.9990$) for linear Langmuir listed in Table S9) values reflect good fitting of experimental data towards Langmuir isotherm, which indicates that once H₂ molecules occupy homogeneously the sites on the surface of adsorbent, the adsorption is terminated and as consequence the monolayer of H₂ is obtained.

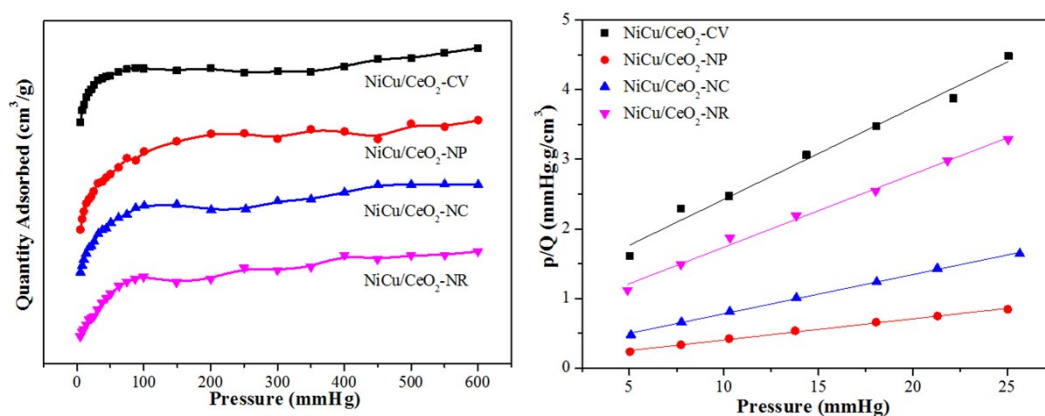


Figure S17. The isotherms of H₂ adsorption as the function of pressure over catalysts.

Table S9 Langmuir adsorption isothermal constants, correlation coefficients and the adsorption capacities of NiCu/CeO₂ samples for H₂ molecular.

Samples	Ni-Cu/CeO ₂ -CV	Ni-Cu/CeO ₂ -NP	Ni-Cu/CeO ₂ -NC	Ni-Cu/CeO ₂ -NR
R ²	0.9829	0.9957	0.9982	0.9930

V_m ($\text{cm}^3 \cdot \text{g}^{-1}$)	7.7	33.0	19.9	10.3
H/metal ratio	1.1	2.6	1.9	1.3
Total active surface areas ($\text{m}^2 \cdot \text{g}^{-1}$)	13.5	58.0	34.9	18.1

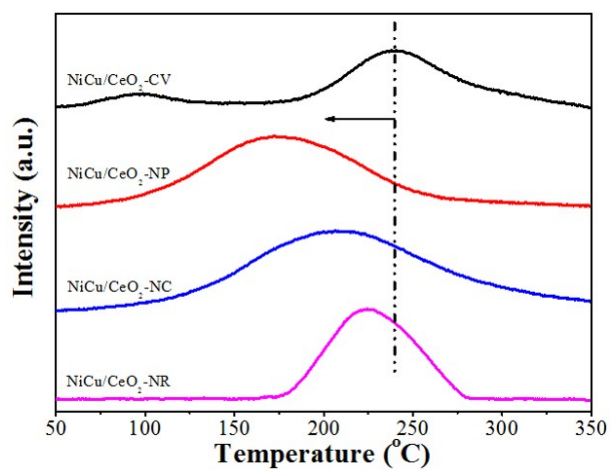


Figure S18. H₂-TPD of Ni-Cu/CeO₂-CV, Ni-Cu/CeO₂-NP, Ni-Cu/CeO₂-NC and Ni-Cu/CeO₂-NR.

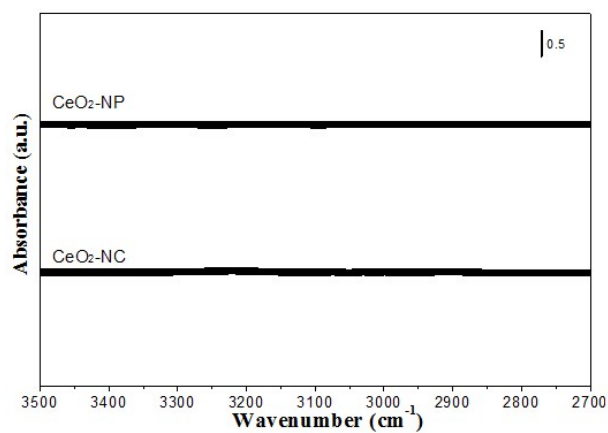


Figure S19. In situ C₂H₂-IR of CeO₂-NP and CeO₂-NC.

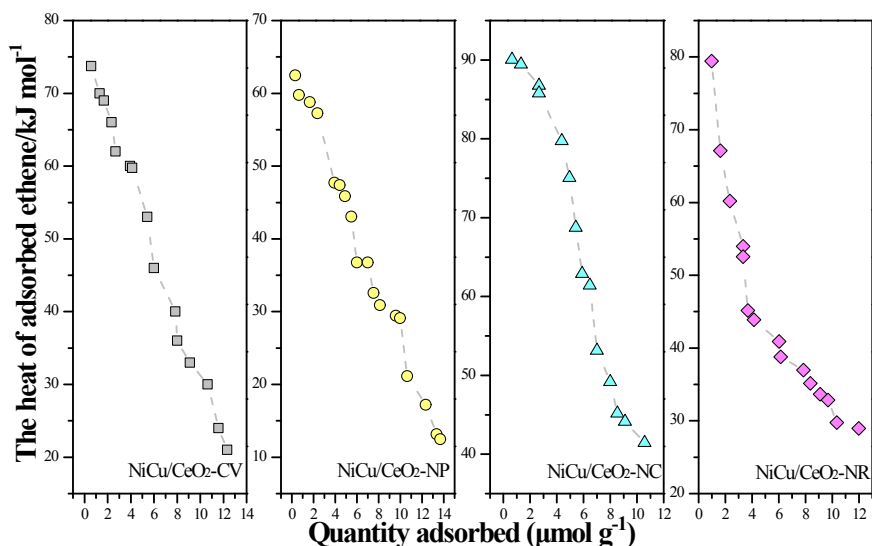


Figure S20. Differential heat of adsorption of C_2H_4 over Ni-Cu/CeO₂ as a function of exposed facets.

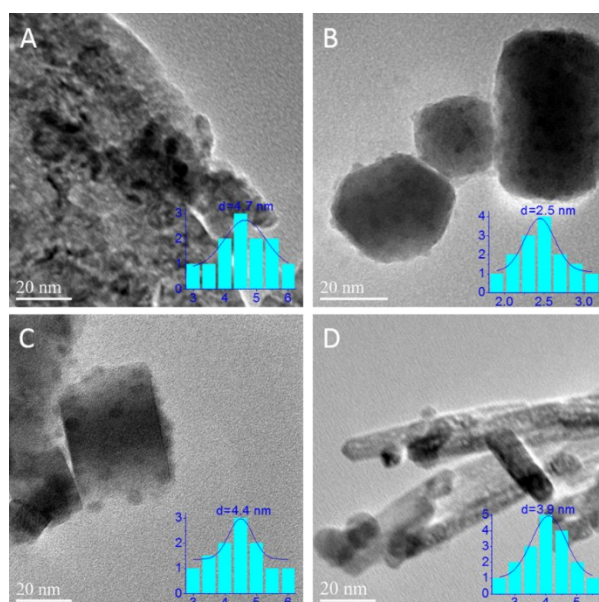


Figure S21. HRTEM images of used catalysts (A) Ni-Cu/CeO₂-CV, (B) Ni-Cu/CeO₂-NP, (C) Ni-Cu/CeO₂-NC, (D) Ni-Cu/CeO₂-NR and the distribution of particle size in the inset.

References

1. S. Maensiri, C. Masingboon, P. Laokul, W. Jareonboon, V. Promarak, P. L. Anderson, S. Seraphin, *Cryst. Growth Des.* 2007, **7** (5), 950–955.
2. L. D. Rogatis, T. Montini, B. Lorenzut, Paolo. Fornasiero, *Energy Environ. Sci.* 2008, **1**, 501–509.
3. Z. L. Yuan, L. Wang, J. H. Wang, S. X. Xia, P. Chen, Z. Y. Hou, X. M. Zheng, *Appl. Catal., B* 2011, **101**, 431–440.
4. Y. N. Liu, J. Y. Zhao, J. T. Feng, Y. F. He, Y. Y. Du, D. Q. Li, *J. Catal.* 2008, **359**, 251–260.

-
5. J. Pérez-Ramírez, B. Bridier, *J. Am. Chem. Soc.* 2010, **132**, 4321–4327.
 6. S. Abelló, D. Verboekend, B. Bridier, J. Pérez-Ramírez, *J. Catal.* 2008, **259**, 85–95.
 7. C. S. Spanjers, J. T. Held, M. J. Jones, D. D. Stanley, R. S. Sim, M. J. Janik, R. M. Rioux, *J. Catal.* 2014, **316**, 164–173.
 8. D. L. Trimm, N. W. Cant, I. O. Y. Liu, *Catal. Today* 2011, **178**, 181–186.
 9. D. L. Trimm, I. O. Y. Liu, N. W. Cant, *Appl. Catal., A* 2010, **374**, 58–64.
 10. C. Guimon, *Appl. Catal., A* 2003, **251**, 199–214.
 11. M. Crespo-Quesada, R. R. Dykeman, G. Laurenczy, P. J. Dyson, L. Kiwi-Minsker, *J. Catal.* 2011, **279**, 66–74.
 12. J. A. Anderson, J. Mellor, R. P. K. Wells, *J. Catal.* 2009, **261**, 208–216.
 13. N. Semagina, A. Renken, L. Kiwi-Minsker, *J. Phys. Chem. C* 2007, **111**, 13933–13937.
 14. B. Tanhaei, A. Ayati, M. Lahtinen, M. Sillanpää, *Chem. Engineer. J.*, 2015, **259**, 1–10.